Eur. Phys. J. D **62**, 25–31 (2011)
DOI: 10.1140/epjd/e2010-10328-3

THE EUROPEAN PHYSICAL JOURNAL D

Regular Article

Faraday patterns in lubricated thin films

N.O. Rojas[1], M. Argentina[1,a], E. Cerda[2], and E. Tirapegui[3]

[1] Université de Nice Sophia Antipolis, Laboratoire J.A. Dieudonné, Parc Valrose, 06108 Nice Cedex 2, France
[2] Departamento de Física, Universidad de Santiago, Av. Ecuador 3493, Santiago, Chile
[3] Departamento de Física, Facultad de Ciencias Físicas y Matematicas, Universidad de Chile, Av. Blanco Encalada 2008, Santiago, Chile

Received 31 May 2010 / Received in final form 14 October 2010
Published online 3rd December 2010 –

Abstract. We study the patterns observed in the vicinity of a Faraday instability, in the limit of a very thin layer of viscous fluid. We numerically solve our previous model [N.O. Rojas et al., Phys. Rev. Lett. **104**, 187801 (2010)] and compare our predictions to experiments. Our model captures quantitatively the threshold of instability. The direct simulation of our system permits us to predict the patterns observed in experiments.

1 Introduction

In this work, we investigate the nonlinear behavior associated to the Faraday instability [2]. It is related to the appearance of patterns on the surface of a fluid whose container is shaken vertically and periodically. This phenomenon can be easily observed by rubbing a glass of polystyrene filled with water on a rough surface with an appropriate velocity: small wavelets appear at the surface of the fluid. This research field was probably initiated by Hooke who, after having deposited some flour on a thin glass plate, ran a violin bow on its section and reported the appearance of patterns of density of the grains [3]. Chladni, author of the first treaty concerning the science of acoustics [4] established the relation between the distribution of the granular material and the vibration modes of the plate. By extending the previous experiments to a fluid deposited on a vibrating plate, Faraday observed the formation of small waves oscillating at half the frequency of the vibrations imposed on the container. The observations of Faraday, although discussed at the time, were then confirmed by the work of Lord Rayleigh [5]. The first theoretical description was proposed much later for non-viscous fluids [6]. In this limit, the authors derived a Mathieu equation to describe the thickness of the vibrated fluid. Note that Mathieu wrote his equation in the study of the dynamics of a vibrated elliptic plate [7].

Benjamin and Ursell wrote the deformation ξ of the fluid surface in the shallow water limit, i.e. when the fluid at rest has a thickness h much smaller than the wavelength $2\pi/k$ of the surface deformation. These waves, of amplitude ξ_k, oscillate in time with a frequency proportional to $\sqrt{gk}$:

$$\ddot{\xi}_k + gk\xi_k = 0. \tag{1}$$

This equation is presented in numerous textbooks for describing free surface flows [8]. However, in the reference frame of the vibrated container, this system depends on time since the gravitational acceleration is modified into $g(t) = g + a(t)$, where $a(t)$ is the forcing acceleration. Consequently, we get:

$$\ddot{\xi}_k + gk\left(1 + \frac{a(t)}{g}\right)\xi_k = 0, \tag{2}$$

which becomes the Mathieu equation with a harmonic function $a(t)$. Despite the beauty and the simplicity of this parametrically forced oscillator, it does not predict the observed wavelength for common fluids like water or oil, because viscosity plays a particular role as it selects the wavelength of the instability. The appearance of these viscous patterns have been described in numerous experiments [9,10]. In order to supplement the previous model, it was necessary to take into account dissipation effects. The first approach consisted in adding a term $1/\tau\dot{\xi}_k$ to equation (2), where τ is a characteristic time which depends on the dynamic viscosity ν of the fluid. On one hand, for large thickness, this characteristic damping timescale is $\tau \sim 1/(\nu k^2)$, and for thin film experiments, $\tau \sim h^2/\nu$. From a theoretical point of view, the inclusion of viscosity has been achieved in amplitude equations [11], or by a direct numerical analysis of the Navier-Stokes equations [12,13]. The formal inclusion of the viscosity in the models was proposed only at the end of the nineties in several works (see review [14,15]) that predicted successfully the instability thresholds measured in experiments.

[a] e-mail: mederic.argentina@unice.fr

However these approaches, although powerful, remained limited to linear stability analysis. Amplitude equations have been derived [16] to catch the weakly nonlinear regime. In addition, they have been a recent three dimensional nonlinear numerical simulations of the full Faraday problem [17] that explored the nonlinear phenomena of the Faraday instability.

In our previous work [1], we have been interested in the nonlinear aspects related to this instability. We derived equations describing the position of the interface and the two horizontal mass fluxes for thin and viscous films. In the next section, we briefly present our previous model. We later explain our results concerning the patterns observed in parameter space where harmonic and subharmonic responses co-exist. We compare our prediction to experimental measurements [18].

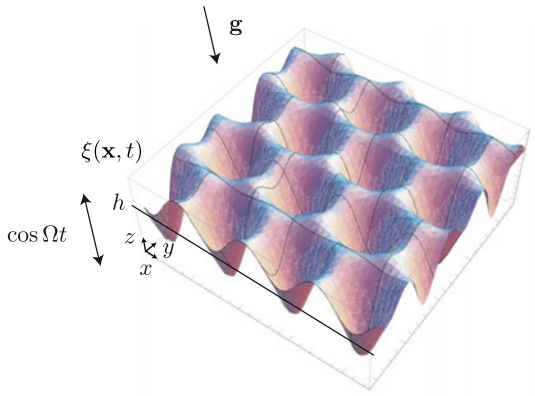

Fig. 1. (Color online) Numerical simulation of the free surface using our model (4), (5) with physical parameters given in experiments [18]. Hexagonal structures are observed.

2 Presentation of our model

We consider a thin film of an incompressible viscous fluid described by the Navier-Stokes equations. The ratio between the characteristic lengths of the problem is $\epsilon = \frac{h}{L}$ where h is the thickness of the fluid and L is the typical horizontal length. The viscous limit is obtained by taking the Reynolds number $Re = \frac{\Omega h^2}{\nu}$ to be small, where ν is the dynamical viscosity of the fluid. The container is accelerated periodically and vertically at a frequency Ω and an amplitude a. In the asymptotics of $Re \ll 1$ and $\epsilon \ll 1$, the inertial effects and the small aspect ratio are taken into account as a perturbation of the Reynolds equation:

$$\partial_t \xi + \nabla_\perp \left(\frac{\xi^3}{3\nu}(g(t) - \frac{\gamma}{\rho}\nabla_\perp^2)\nabla_\perp \xi \right) = \mathcal{O}(Re, \epsilon). \quad (3)$$

The free surface position is located at $z = \xi(\mathbf{x}, t)$, as seen in Figure 1, the surface tension on the liquid-air interface is measured with γ and ρ is the density of the fluid. The operator $\nabla_\perp$ represents the operator gradient with respect to the horizontal variables x and y. The perturbed equations of the free surface is obtained with a Taylor series expansion of the vertical variable with $z \ll 1$, on the velocity field and the pressure [1]. The small aspect ratio ϵ approximation, joined with low Reynolds limit, permit us to find explicitly the two following closed relations for ξ and the horizontal mass fluxes $\mathbf{q}(\mathbf{x}, t)$:

$$\partial_t \xi + \nabla_\perp \cdot \mathbf{q} = 0, \quad (4)$$

$$Re\mathcal{E}(\xi, \mathbf{q}) + \epsilon^2 \mathcal{F}(\xi, \mathbf{q}) + 3\mathbf{q} + \xi^3 (G - B\nabla_\perp^2)\nabla_\perp \xi = 0, \quad (5)$$

written in a dimensionless form. Equation (4) represents the mass conservation, whereas equation (5) is related to horizontal momentum conservation. For the nondimensionalization, we use as a horizontal length scale L, as vertical one h, and the time scale is chosen to be $1/\Omega$. We have introduced two new parameters: $G = gh^3/\nu\Omega L^2$ which is a dimensionless gravity parameter and $B = \gamma h^3/\rho\nu\Omega L^4$ the scaled surface tension. The Weber number which predicts the capillarity length, is given by $W = G/B$. Finally, we give the functions $\mathcal{E}$ and $\mathcal{F}$:

$$\mathcal{E} = \frac{6}{5}\left[\left(\xi^3\partial_t + \frac{9}{7}\xi^2(\mathbf{q}\cdot\nabla_\perp)\right)\left(\frac{\mathbf{q}}{\xi}\right) + \frac{1}{7}\xi\mathbf{q}(\nabla_\perp\cdot\mathbf{q})\right]$$

$$\mathcal{F} = -\frac{3}{2}\left[-\xi^2\mathbf{A} + \xi^3\nabla_\perp\left(\nabla_\perp\cdot\left(\frac{\mathbf{q}}{\xi^2}\right)\right) + \mathbf{B}\right]$$

$$\mathbf{A} = -\nabla_\perp(\nabla_\perp\cdot\mathbf{q}) + \frac{3}{2}\left[\frac{\mathbf{q}}{\xi}, \nabla_\perp\xi\right] - \frac{3}{2}\nabla_\perp\xi\left(\nabla_\perp\cdot\left(\frac{\mathbf{q}}{\xi}\right)\right)$$

$$\mathbf{B} = \frac{5\xi^4}{4}\left[\nabla_\perp^2\left(\frac{\mathbf{q}}{\xi^2}\right) + \nabla_\perp\left(\nabla_\perp\cdot\left(\frac{\mathbf{q}}{\xi^2}\right)\right)\right] - \frac{9\xi^5}{10}\nabla_\perp^2\left(\frac{\mathbf{q}}{\xi^3}\right),$$

where $[\cdot,\cdot]$ is the Lie bracket.

The Faraday instability threshold can be deduced from our model by studying the dynamics of the perturbations $\tilde{\xi}$ of ξ and those of the flows around the equilibrium position $\xi = 1$ and $\mathbf{q} = \mathbf{0}$:

$$\frac{6}{5}Re\,\partial_t^2\tilde{\xi} + \left(3 - \frac{27}{5}\nabla_\perp^2\right)\partial_t\tilde{\xi} - (G(t) - B\nabla_\perp^2)\nabla_\perp^2\tilde{\xi} = 0. \quad (6)$$

Here we have chosen, without loss of generality, $L = h$, see [1] for details. We obtain a damped Mathieu equation, by assuming that $\xi \sim \xi_k e^{ikx}$:

$$\frac{6}{5}Re\,\partial_t^2\tilde{\xi}_k + \left(3 + \frac{27}{5}k^2\right)\partial_t\tilde{\xi}_k + k^2(G(t) + Bk^2)\tilde{\xi}_k = 0, \quad (7)$$

that recovers the previous results of linear theory on viscous flows [12,15] in the limit of thin lubricated films.

3 Comparison with experiments

In this section, we compare our model to experiments. We first compare the instability thresholds. By simulating equations (4), (5), we later compare the nonlinear patterns of the model to those observed in experiments [18].

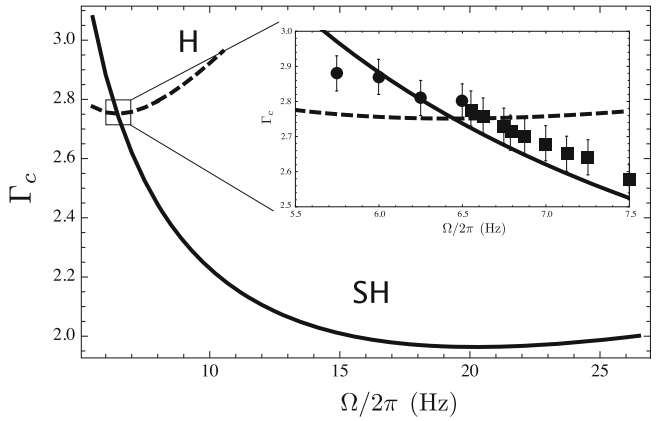

Fig. 2. Harmonic (dashed line) and subharmonic (thick line) critical acceleration Γ_c versus the frequency forcing $f = \Omega/2\pi$. Inset: comparison with experiments. The disks (resp. squares) represent the harmonic (resp. subharmonic) experimental thresholds [18].

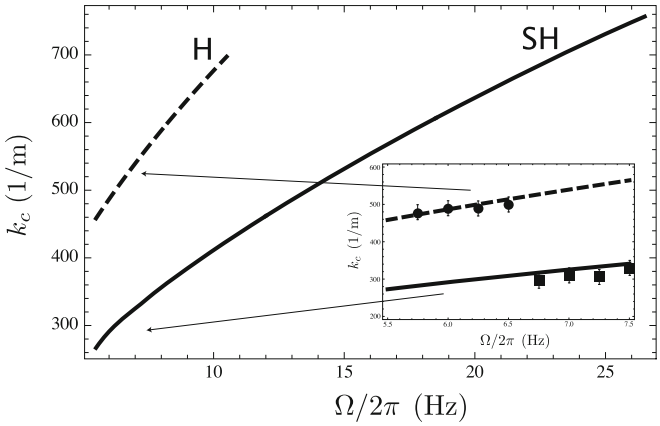

Fig. 3. Harmonic (dashed line) and subharmonic (thick line) critical wavenumber versus the frequency forcing $f = \Omega/2\pi$. Inset: comparison with experiments. The disks (resp. squares) represent the harmonic (resp. subharmonic) experimental wavenumbers [18].

3.1 Instability thresholds

We follow the aforementioned experiments, by using a harmonic forcing $G(t) = G(1+\Gamma\cos t)$. We perform a numerical Floquet analysis to find the threshold of the Faraday instability. By solving equation (7) with a fourth-order Runge-Kutta scheme, we construct the monodromy matrix M that links the states $(\xi(0), \dot{\xi}(0))$ to $(\xi(2\pi), \dot{\xi}(2\pi))$. The eigenvalues of M are computed. The subharmonic instability is detected as one eigenvalue of M emerges from the unit circle at -1. The harmonic instability is predicted when one eigenvalue of M emerges from the unit circle at 1. Using a Newton algorithm, we compute the critical threshold Γ for a given set of physical parameters (ν, h, etc.). The wavenumber k is still an unknown that needs to be determined. In experiments, the selected wavenumber corresponds to the lowest possible value of Γ. For a given set of parameters, we search for the smallest value Γ_c and its corresponding wavenumber k_c for the harmonic and the sub-harmonic response. In Figures 2 and 3, we present the dependence of Γ_c and k_c as a function of the frequency forcing $f = \Omega/2\pi$, and we compare it to experimental results [18].

3.2 Phase diagrams

We perform direct numerical simulations of the reduced system (4), (5) in order to reproduce experimental results of Wagner et al. [18] for thin viscous fluid layers. The numerical simulations of equations are performed using a staggered mesh [19]. The derivatives are approximated with finite differences, and the temporal scheme is a fourth-order Runge Kutta method [20] with $L = 1$ (cm), $dt = 0.02$ and $dx = 0.1$ using periodic boundary conditions. The mesh is composed of 128×128 points, such that the size of the computational domain is 12.8 and the physical domain is 12.8 (cm). In the Fourier space the domain is 33.1186 (cm^{-1}) due to a zoom carried out in the central region. In all the simulations we fix use the following set of parameter values: $Re = 0.6157f$, $G = 1.07/f$, $B = 0.023/f$, $\epsilon = 0.07$.

For a given value of the frequency, we explore the phase space by ramping the forcing acceleration upwards and downwards. For each point measured in the phase diagram (Fig. 4) we performed a spatiotemporal diagram in order to determine whether a pattern is harmonic or subharmonic which is indicated with the labels **h** and **sh** respectively.

We observe a strong hysteresis that depends on the way physical parameters are changed. Two different sequences have been performed: this is why we present two phase diagrams. For the first one, we start the measurements from the subharmonic threshold (see Fig. 4a), whereas for the second one, we start the simulations from the harmonic threshold (see Fig. 4b). In both cases, random initial conditions were used. The thick curves of the experiments separates regions with different Fourier spectras. The regions predicted by our model are plotted in dashed lines. The phase diagram in Figure 4 appears to be in very good agreement with experimental results. Numerical and experimental measurements in Figure 4 were obtained by increasing the external acceleration Γ.

Metastable regions can be deduced with a superposition of Figures 4a and 4b. Hysteresis is also present when acceleration is taken downwards: for sake of simplicity, we chose to not discuss this aspect. There is a region in Figure 4a, extending from $f = 6.5$ (Hz) to $f = 6.75$ (Hz), where a transition from sub-harmonic squares to harmonic hexagons can be observed.

In the next section, we present in more detail the phase diagram and the observed patterns.

3.3 Fourier analysis

In order to classify the different patterns obtained for each frequency and acceleration, we use a Fourier analysis.

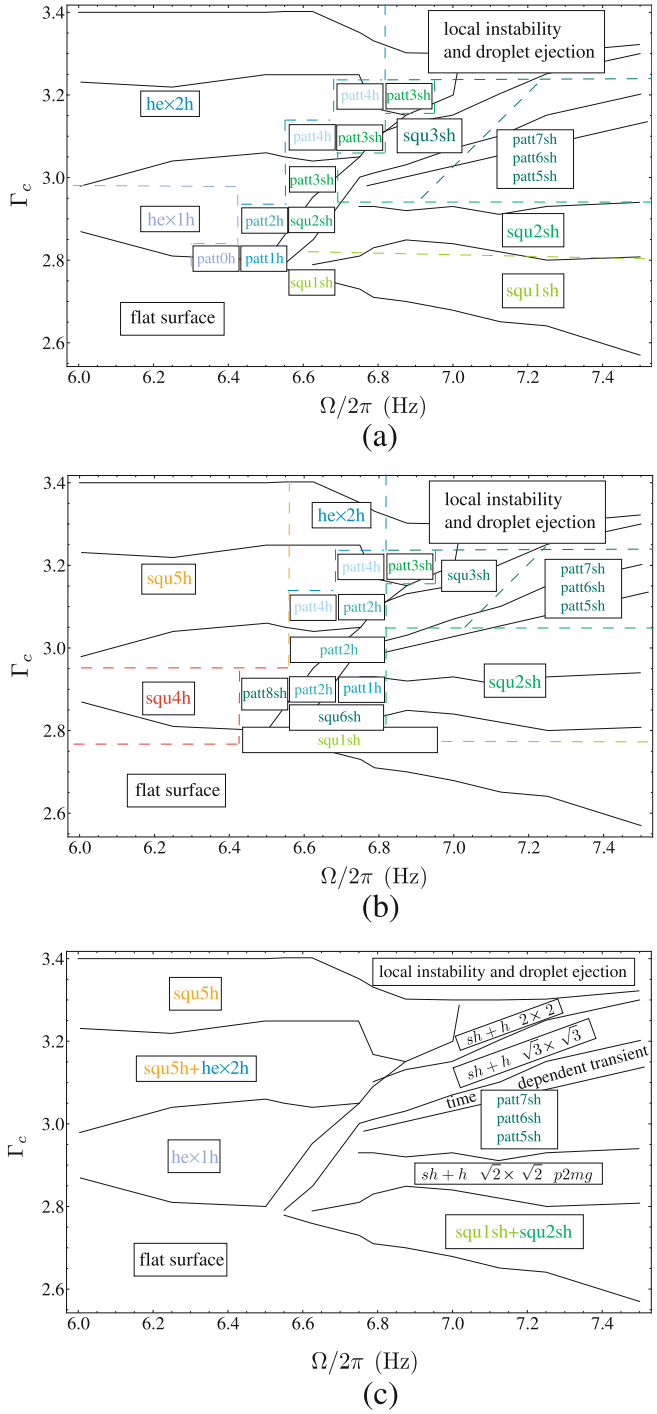

Fig. 4. (Color online) Phase diagram around the bi-critical point between harmonic and sub-harmonic tongues. The thick lines have been measured experimentally in [18]. The dashed lines are the numerical predictions using our model. Numerical and experimental measurements were taken by ramping up the external acceleration Γ from the subharmonic tongue (a) and the harmonic tongue (b). The patterns are labelled with a code composed of ten characters. The labels starting by squ and hex represent respectively square and hexagonal patterns. (c) Experimental phase diagram [18] identified with our notation. The (sub) harmonic response is noted by the latter(s) $(s)h$ at the end of the label code. The parameters are $Re = 0.6157f$, $G = 1.07/f$, $B = 0.023/f$, $\epsilon = 0.07$.

Since our computational domain is doubly periodic, we numerically compute the Fourier series from the deformation field ξ. Fourier spectra was calculated by taking the surface height for each mesh point at a maximum $t = 2\pi/\Omega$ ($t = 4\pi/\Omega$) in the (sub)harmonic case. The Fourier transforms where performed using Mathematica. Numerical simulations have been run until a asymptotic regime is attained. We use a simple algorithm which calculates the distance of each peak to the center in the Fourier space and its amplitude. For a given distance, the number of peaks in the Fourier domain is evaluated: this permits to differentiate the square patterns (for which four peaks are present) from hexagonal structures (six peaks). The results of this analysis are reported in Figure 4.

3.3.1 Ramping from the subharmonic threshold

We choose a frequency and its corresponding critical acceleration Γ_c at the subharmonic threshold (for example from Fig. 2). From this starting point, we increase adiabatically Γ. We observe a region with hexagonal patterns for 6 (Hz) $< f \leq f_b \approx 6.5$ (Hz) and a region of square-type patterns for $f > f_b$, both of them separated by an area with complex spatial structure. As usual, as the forcing is increased, nonlinearities create supplementary modes. f_b corresponds to the frequency for which the harmonic and sub-harmonic marginal curve coincides.

For 6.5 (Hz) $< f <$ 6.75 (Hz), a square-hexagon transition can be seen. As an example, we give an overview of this transition at $f = 6.625$ (Hz) in Figure 5. Starting from subharmonic oscillating squares (Fig. 5a) for $\Gamma = 2.8$, a transition to a quadratic $\sqrt{2} \times \sqrt{2}$ superlattice (Fig. 5b) is reached at $\Gamma = 3.0$. A further increase in Γ to 3.1 provokes a strong distorsion of the lattice (Fig. 5c). Finally, a pure hexagonal tiling (Fig. 5d) is observed at $\Gamma = 3.3$.

For 6.8 (Hz) $< f <$ 7.5 (Hz), subharmonic squares evolve into a $\sqrt{2} \times \sqrt{2}$ superlattice as explained in [18]. An example at $f = 7.125$ (Hz) is given in Figure 6.

3.3.2 Ramping from the harmonic threshold

In this case, the measurements are recorded by starting from the harmonic tongue. For 6.0 (Hz) $< f <$ 6.5 (Hz), harmonic squares are found.

From $f = 6.5$ (Hz) to $f = 7.5$ (Hz), the phase diagram is similar to the previous case and no bistability is observed (see Fig. 4b).

For high values of Γ, before droplet ejection, the fluid surface increases its amplitude and becomes multivalued which is obviously not allowed for the function $\xi(\mathbf{x}, t)$. In this region, our model loses its validity.

3.3.3 Patterns

In this subsection, we explain the different patterns observed in the phase diagrams. For the description of the Fourier spectra, we use the notations used in the experiments [18].

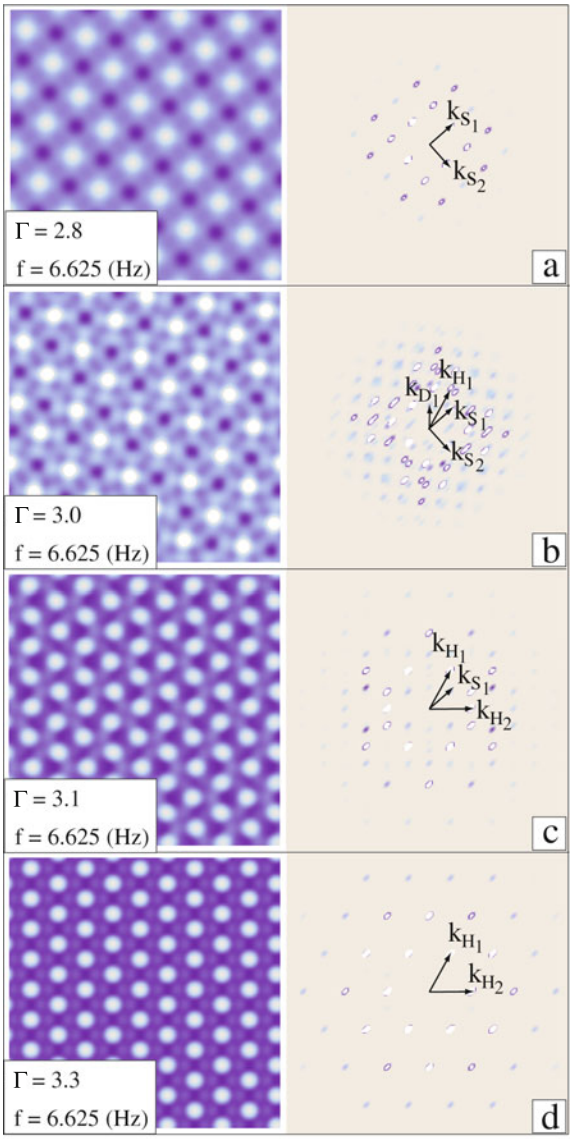

Fig. 5. (Color online) Square-hexagon transition: ξ (left) and its Fourier spectra (right). (a) squ1sh (b) patt3sh (c) patt4h (d) hex2h. White dots on the Fourier transforms have bigger amplitude than dark dots.

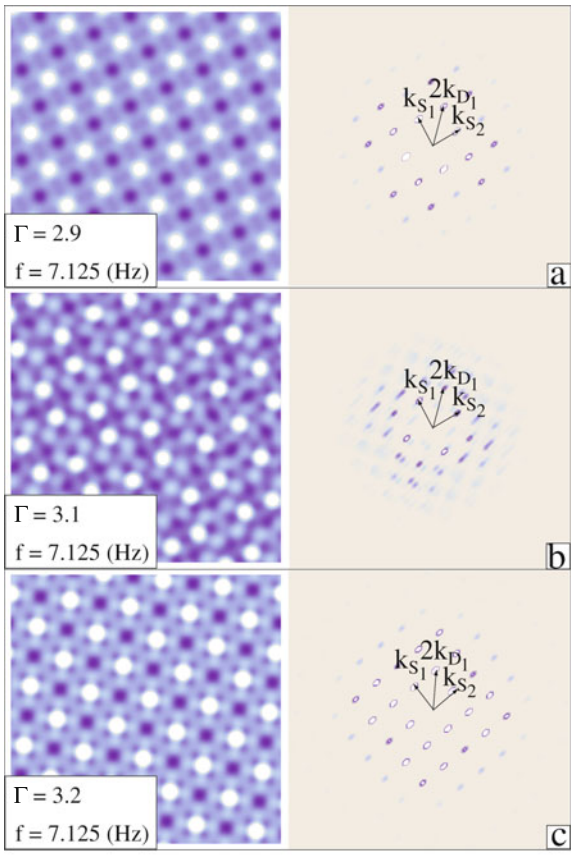

Fig. 6. (Color online) Squares pattern: ξ (left) and Fourier spectra (right) (a) squ2sh (b) patt6sh (c) squ3sh.

Harmonic hexagons

They are found at frequencies lower than $f_b \approx 6.5$ (Hz) when the measurements are started from the sub-harmonic tongue (see Fig. 2a inset): the basin of attraction of the harmonic response is larger near this threshold, because the parameter regime is far away from the harmonic marginal stability curve (see Fig. 2).

Increasing the acceleration Γ, hexagonal structures are observed also at $f > f_b$ for higher accelerations. Hexagons hex1h and hex2h of Figure 4 are classified according to the number of excited modes in the Fourier spectra, which increase with the forcing magnitude: each appearance is plotted in dashed line of the phase diagram of Figure 4a. Typical wave vectors associated to hexagonal structures are named $\mathbf{k}_{H_i}$ as shown in Figure 5d for $f = 6.625$ (Hz) and $\Gamma = 3.3$. The angle separating the two vectors $\mathbf{k}_{H_1}$ and $\mathbf{k}_{H_2}$ is 60°.

Sub-harmonic Squares

Sub-harmonic oscillating squares (see Fig. 5a) are always found at frequencies higher than f_b composed of the two fundamental wave vectors $\mathbf{k}_{S_1}$ and $\mathbf{k}_{S_2}$, separated by an angle of 90°. Increasing the drive strength Γ, $\mathbf{k}_D$ and $\mathbf{k}_H$ wave vectors are generated as shown in Figure 5b (pattern 3). We have $|\mathbf{k}_{D_i}| = \sqrt{2}/2|\mathbf{k}_{S_i}|$. From Figure 3, it is possible to calculate the ratio between the subharmonic (squares $|\mathbf{k}_S| = k_c^s$) and harmonic (hexagons $|\mathbf{k}_H| = k_c^h$) critical wavenumbers $k_c^h/k_c^s \sim 1.58$. Modes $|\mathbf{k}_D|$ act as mediators, enabling the resonance between S and H modes according to the geometrical rules $\mathbf{k}_{H_1} = \mathbf{k}_{S_1} + \mathbf{k}_{D_1}$ as shown in Figure 5b (patt3h). The angle between the two vector $\mathbf{k}_{S_1}$ and $\mathbf{k}_{D_1}$ is 45°.

Sub-harmonic square patterns squ1sh, squ2sh, squ3sh in the phase diagrams 4a and 4b are classified according to the number of excited modes as shown in Figures 5a for squ1sh, Figure 6a for squ2sh and Figure 6c for squ3sh.

Harmonic squares

These structures are found for low frequencies ($f < f_b$) when the measurements are started near the harmonic

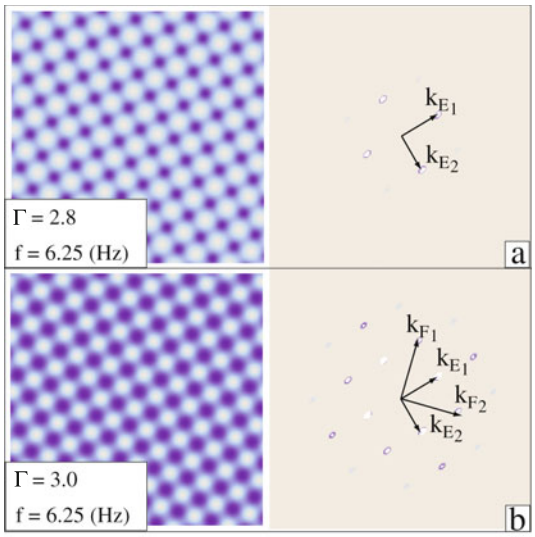

Fig. 7. (Color online) Harmonic squares: free surface ξ (left) and Fourier spectra (right) (a) squ4h (b) squ5h.

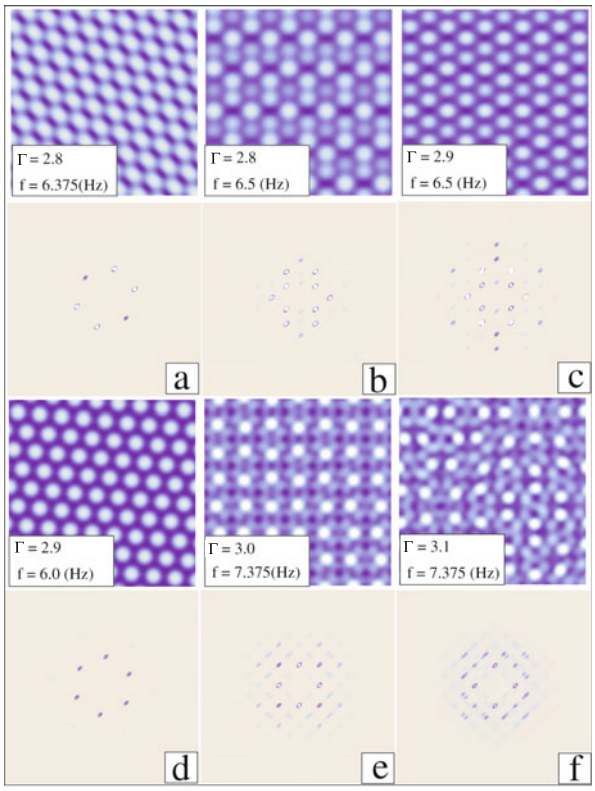

Fig. 8. (Color online) Diverse structures found in the phase diagrams of Figures 4. In this caption, we just give the label of the pattern, their description will be found in the text. (a) patt0h (b) patt1h (c) patt2h (d) hex1h (e) patt5sh (f) patt7sh.

tongue. Basic wave vectors $\mathbf{k}_E$, that define the square patterns, are bigger in magnitude than the subharmonic square wavenumber $|\mathbf{k}_S|$. The angle between $\mathbf{k}_{E_1}$ and $\mathbf{k}_{E_2}$ is 90°. While increasing the forcing amplitude other modes are excited as shown in Figure 7. The first excited modes

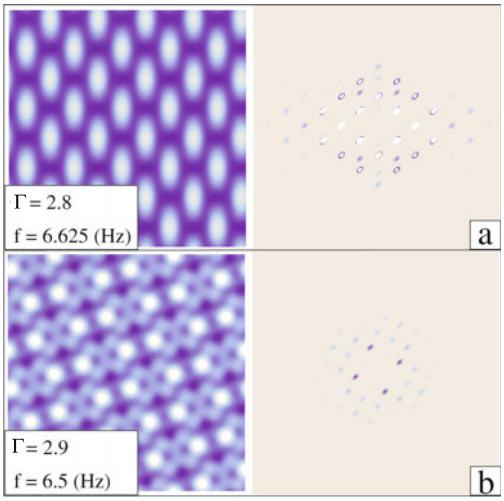

Fig. 9. (Color online) Patterns found in phase diagram 4. (a) squ6sh (b) patt8sh.

have a wavevector $\mathbf{k}_{F_i}$. Due to quadratic nonlinearities, $\mathbf{k}_{E_i}$ and $\mathbf{k}_{F_i}$ modes follows the rule $\mathbf{k}_{F_2} = \mathbf{k}_{E_1} + \mathbf{k}_{E_2}$ (see Fig. 7b). In the phase diagram Figures 4a and 4b, we differentiate the patterns squ4sh and squ5sh by the number of excited modes in the Fourier space.

Stationary structures

Besides hexagons and squares, many different patterns with complex structures are found. As seen in Figure 8, they have all different forms in real and Fourier space.

- The rhomboid like pattern patt0h is shown in Figure 8a. The Fourier analysis shows a symmetry breaking on the hexagonal mesh due to the influence of the subharmonic tongue.
- The pattern patt1h is shown in Figure 8b. It looks roughly like a quasi crystalline structure, because its Fourier transforms shows 12 peaks almost located at the same distance from the origin.
- In Figure 8c, we present the pattern patt2h, observed in the transition between squares and hexagons.
- patt5sh, which is shown in Figure 8e is similar to squ2sh in the transition to other structures like patt6sh (Fig. 6b) and patt7sh (Fig. 8f).
- Some patterns found starting from the harmonic threshold are squ6sh (Fig. 9a) and patt8sh (Fig. 9b).

patt3sh and patt4sh can be seen in Figures 5b and 5c as indicated previously.

4 Conclusion

In this work, we study numerically our model for a thin viscous layer of a Newtonian fluid, whose container is forced to oscillate to a given frequency. The threshold of instability together with its critical wavenumber, observed on the free surface, are well predicted by the set of

equations (4), (5). The experimental patterns are reproduced faithfully and the quantitative agreement between the phase diagram of our approach and the experiments confirm the ability of our model to capture accurately the physics of this instability.

N.R. is grateful for the financial support of CONICYT. E.C. and E.T. acknowledge the support of Anillo Act No. 15. E.C. thanks Fondecyt Project No. 1095112. Simulations were done using the XDIM Software developed by M. Monticelli and P. Coullet.

References

1. N.O. Rojas, M. Argentina, E. Cerda, E. Tirapegui, Phys. Rev. Lett. **104**, 187801 (2010)
2. M. Faraday, Philos. Trans. R. London **52**, 319 (1831)
3. *Oxford Dictionary of Scientists* (Oxford University Press, 1999)
4. E.F.F. Chladni, *Die akustik* (Breitkopf und Härtel, Leipzig, 1802)
5. L. Rayleigh, Philos. Mag. **5**, 229 (1883)
6. T.B. Benjamin, F. Ursell, Series A, Math. Phys. Sci. **225**, 505 (1953)
7. E. Mathieu, J. Math. Pure Appl. **13**, 137 (1868)
8. L.D. Landau, E.M. Lifshitz, *Fluid Mechanics* (Pergamon, 1987)
9. S. Douady, S. Fauve, Europhys. Lett. **6**, 221 (1988)
10. W.S. Edwards, S. Fauve, Phys. Rev. E **47**, R788 (1993)
11. S.T. Milner, J. Fluid. Mech. **225**, 81 (1991)
12. K. Kumar, L. Tuckerman, J. Fluid. Mech. **279**, 49 (1994)
13. J. Beyer, R. Friedrich, Phys. Rev. E **51**, 1162 (1995)
14. F.J. Mancebo, J.M. Vega, J. Fluid. Mech. **467**, 307 (2002)
15. E.A. Cerda, E.L. Tirapegui, J. Fluid. Mech. **368**, 195 (1998)
16. P. Chen, J. Viñals, Phys. Rev. E. **60**, 551 (1999)
17. N. Perinet, D. Juric, L.S. Tuckerman, J. Fluid. Mech. **635**, 126 (2009)
18. C. Wagner, H.W. Müller, K. Knorr, Phys. Rev. E **68**, 066204 (2003)
19. S.V. Patankar, *Numerical Heat Transfer and Fluid Flow* (Taylor and Francis, 1980)
20. W.H. Press, S.A. Teukolsky, W.T. Vetterling, B.P. Flannery, *Numerical Recipes in C: The Art of Scientific Computing* (Cambrigde University Press, New York, 1992)
21. K. Kumar, Proc. R. Soc. London A **452**, 1113 (1996)
22. P.C. Newell, A.C. Passot, J. Lega, Ann. Rev. Fluid Mech. **25**, 399 (1993)
23. W. Zhang, J. Viñals, J. Fluid Mech. **336**, 301 (1997)
24. M.C. Cross, P. Hohenberg, Rev. Mod. Phys. **65**, 851 (1996)